A positivity-preserving semi-implicit discontinuous Galerkin scheme for solving extended magnetohydrodynamics equations

Xuan Zhao [a], Yang Yang [b], Charles E. Seyler [a,*]

[a] *School of Electrical and Computer Engineering, Cornell University, Ithaca, NY 14853, USA*
[b] *Department of Mathematical Science, Michigan Technological University, Houghton, MI 49931, USA*

A R T I C L E   I N F O

A B S T R A C T

A positivity-preserving discontinuous Galerkin (DG) scheme [42] is used to solve the Extended Magnetohydrodynamics (XMHD) model, which is a two-fluid model expressed with a center-of-mass formulation. We prove that DG scheme with a positivity-preserving limiter is stable for the system governed by the XMHD model or the resistive MHD model. We use the relaxation system formulation [28] for describing the XMHD model, and solve the equations using a split level implicit–explicit time advance scheme, stepping over the time step constraint imposed by the stiff source terms. The magnetic field is represented in an exact locally divergence-free form of DG [23], which greatly improves the accuracy and stability of MHD simulations. As presently constructed, the method is able to handle a wide range of density variations, solve XMHD model on MHD time scales, and provide greatly improved accuracy over a Finite Volume implementation of the same model.

1. Introduction

In High Energy Density (HED) plasma systems, we usually must deal with a wide dynamic range of current carrying densities. When density is so low that the scale lengths are comparable to ion inertial length, the single fluid model would break down. For these problems two-fluid physics is essential, but the applicability of existing numerical methods [6,16,17,19,25,34] in this plasma regime is still limited. In this paper we develop a discontinuous Galerkin (DG) method to solve an extended Magnetohydrodynamics (XMHD) model based on a relaxation formulation, and will demonstrate that this numerical scheme has high accuracy, is computationally efficient, and can handle the large dynamic density range for HED plasmas.

DG schemes are widely used in the hyperbolic algorithms community, since the method can handle complex geometries, has an arbitrary order of accuracy, and is efficient in parallel calculations [9–12,31]. In addition, DG has further advantages for HED plasmas, because the density range is very wide, one often faces a problem where the initial density profile is nearly a δ-singularity (e.g. a pinched-down wire). Such problems are difficult to approximate numerically, and most previous techniques are based on the modification of the singularities with smooth kernels in some narrow region (e.g. [37,40] and the references therein), and hence smear such singularities. However, DG methods depend on the weak form of the equations and can solve such problems without modification, leading to a very accurate result [38]. The main challenge

with DG implementations lies in preserving the stability of the system. Near discontinuities, strong oscillations often appear that might send the physically positive quantities negative. When this occurs, the numerical simulation may break down. In our system, the quantities that should be preserved positive are: density ρ, pressure P, energy $\mathcal{E}$. To ensure these quantities satisfy a positivity-preserving property, one could use a Total Variation Diminishing (TVD) scheme; however all TVD schemes will degenerate to lower order accuracy at smooth extrema [41]. In [42], a positivity-preserving high order DG scheme is developed for solving the compressible Euler equations, and in [39], the authors demonstrated the L^1-stability of such a scheme. This scheme has been applied on solving the ideal magnetohydrodynamic (MHD) equations [3,7]. In this paper, we will demonstrate that the positivity-preserving DG scheme can establish a positivity-preserving property for a system described by an XMHD model or a resistive MHD model, thus preserving the stability of the system.

For solving the XMHD model, we use the relaxation algorithm proposed in [28] to solve the combination of generalized Ohm's law (GOL) and the Maxwell–Ampére law for the electric field. The relaxation method is essentially a semi-implicit time differencing proven to converge to the solution of the algebraic equations that are the stiff source terms set equal to zero. In the case of XMHD this means the solution converges to GOL in which the electron inertial terms are neglected and to the Maxwell equation in which the displacement current term is neglected (Ampére's Law). Using this algorithm, one can avoid the constraint imposed by the under-resolved stiff source terms to step over electron plasma and cyclotron frequencies, which are often under-resolved in the characteristic regime, and thereby allow one to solve the XMHD equations on MHD time scales. In this algorithm, the Hall term is locally implicit avoiding the substantial effort in solving a large linear system. Furthermore, with XMHD model, in low-density region, the current is suppressed by both Hall and electron inertial terms, one is able to use the unmodified Spitzer resistivity, which makes the plasma–vacuum transition automatic and physical. This algorithm has been implemented into an XMHD code called PERSEUS with a second-order finite volume (FV) scheme. Because of the extended stencil, FV is often too diffusive to characterize small-scale fluid instabilities and to resolve the local details of a shock structure without a large number of cells. On the other hand, DG scheme is more compact in the sense that every cell is treated independently, and the solution is localized within a cell. This leads to a reduced numerical diffusion. In this paper, we compare the performance of a DG formulation XMHD code to that of an FV formulation, and will demonstrate through numerical tests that DG has a significant advantage over the same order of FV in both memory and CPU time. Additionally we compare selected results with those found from the MHD model computed using the same algorithm. This comparison demonstrates the viability of the method for solving XMHD problems as well as to point out important deficiencies in MHD.

This paper is organized as follows. In Section 2 we introduce the XMHD model and the relaxation algorithm. In Section 3, we construct the DG scheme used in this paper, and demonstrate that a positivity-preserving limiter can preserve the positivity-preserving property in a system governed by an XMHD model or a resistive MHD model, we will also give a brief introduction on the implementation of our algorithm. In Section 4, we present the results of numerical tests, in some of the tests, we do a comparison with FV, to show that DG is more accurate and more efficient than an FV implementation. We also give examples of the method applied to fundamental plasma physics problems and provide a comparison with the MHD model for the same problems. Concluding remarks are provided in Section 5.

2. XMHD model

2.1. Governing equations

In the study of HED plasmas, we are often in a regime where the ion inertial length or even the electron inertial length are resolved by the cell dimensions. When this occurs, standard MHD does not accurately describe the system, and a more generalized model is called for. The two-fluid model expressed with a center-of-mass formulation, which is the XMHD model, covers most of the physics occurring in this regime. The primary exception being due to space-charge effects, which is neglected in the quasineutral XMHD model. The XMHD model is given by:

$$\frac{\partial \rho}{\partial t} + \nabla \cdot (\rho \mathbf{u}) = 0 \tag{2.1}$$

$$\frac{\partial}{\partial t}(\rho \mathbf{u}) + \nabla \cdot (\rho \mathbf{uu} + \mathbf{I}P) = \mathbf{J} \times \mathbf{B} \tag{2.2}$$

$$\frac{\partial \mathcal{E}_n}{\partial t} + \nabla \cdot \left[\mathbf{u}(\mathcal{E}_n + P) \right] = \mathbf{u} \cdot (\mathbf{J} \times \mathbf{B}) + \eta \mathbf{J}^2 \tag{2.3}$$

$$\frac{\partial \mathbf{B}}{\partial t} + \nabla \times \mathbf{E} = 0 \tag{2.4}$$

$$\frac{\partial \mathbf{E}}{\partial t} - c^2 \nabla \times \mathbf{B} = -\frac{1}{\epsilon_0} \mathbf{J} \tag{2.5}$$

$$\frac{\partial \mathbf{J}}{\partial t} + \nabla \cdot \left(\mathbf{uJ} + \mathbf{Ju} - \frac{1}{n_e e} \mathbf{JJ} - \frac{e}{m_e} \mathbf{I}P_e \right) = \frac{n_e e^2}{m_e} \left(\mathbf{E} + \mathbf{u} \times \mathbf{B} - \eta \mathbf{J} - \frac{1}{n_e e} \mathbf{J} \times \mathbf{B} \right) \tag{2.6}$$

$$\partial_t S_e + \nabla \cdot (\mathbf{u}_e S_e) = (\gamma - 1) n_e^{1-\gamma} \eta \mathbf{J}^2. \tag{2.7}$$

Where ρ, P, $\mathbf{u} = (u_x, u_y, u_z)$, $\mathcal{E}_n$, $\mathbf{B} = (B_x, B_y, B_z)$, $\mathbf{E} = (E_x, E_y, E_z)$, $\mathbf{J} = (J_x, J_y, J_z)$, and S_e denote the density, pressure, velocity field, the sum of the kinetic and internal energies, magnetic field, electric field, current density, and electron entropy density, respectively. The resistivity is η. We have $q_i = -Zq_e = Ze$, with Z being the net ion charge. With the assumption of quasineutrality and to leading order in m_e/m_i, we have $n_e = Zn_i = nZ$. $\rho = m_i n_i + m_e n_e$, $\mu = Z m_e/m_i$, $\mathbf{u_e} = \mathbf{u} - \mathbf{J}/(n_e e)$, $\mathbf{J} = e(Z n_i \mathbf{u_i} - n_e \mathbf{u_e})$. We also have $P = (\gamma - 1)(\mathcal{E}_n - \rho \mathbf{u}^2/2)$ and $P_e = S_e n_e^{\gamma - 1}$.

We have chosen to model the electron equation of state using the electron entropy density given by $S_e = P_e/n_e^{\gamma - 1}$ because we are unable to prove that the electron pressure will remain positive when the electron energy equation is used. The issue arising in the proof of electron pressure positivity is due to the non-positive nature of the electron energy equation source terms which directly involve the electric field; however, the electron entropy density source term is positive and we can easily prove electron pressure positivity. The proof of positivity of the total pressure is also complicated by the non-positive nature of the total energy source term, but in that case the proof goes through if certain time-step restrictions are applied. The disadvantage of the use of the electron entropy density over the electron energy density is that the entropy density only allows for adiabatic changes in the thermodynamic variables and hence we cannot capture weak solutions in the form of electron shocks. Such circumstances could arise for instance in the form of Langmuir shocks. As we are primarily concerned with low-frequency phenomena, well below the electron plasma frequency, we do not consider the use of the electron entropy density to be a great restriction.

There is also a constraint implied in (2.4). Taking the divergence of (2.4) shows that if $\nabla \cdot \mathbf{B}$ is initially 0, it is always 0. This gives us a constraint $\nabla \cdot \mathbf{B} = 0$. For local preservation of $\nabla \cdot \mathbf{B} = 0$, we use the locally divergence-free DG method [23], which eliminates the need for an expensive divergence cleaning scheme or the use of global divergence-free elements or a global divergence free reconstruction.

By switching off the electron inertia term, electron pressure and the Hall term in Eq. (2.6), we get the resistive MHD model, which is characterized by (2.1)–(2.5), and

$$\mathbf{E} + \mathbf{u} \times \mathbf{B} = \eta \mathbf{J}. \tag{2.8}$$

If not specified, for simplification, MHD model is used to refer to resistive MHD model throughout this paper.

For the class of problems of interest to us XMHD has several important advantages over the two-fluid model. These are: 1. A direct comparison to MHD can be made by simply switching off some terms in Generalized Ohm's Law (2.6); 2. The relaxation method (to be discussed in Section 2.2) can be used to step over the plasma frequency and electron cyclotron frequency when they do not have to be resolved. This greatly reduces the computational cost of XMHD modeling. We have not been successful thus far in implementing a similar scheme for the full two-fluid model. The reason for this is due to finite charge separation which is a topic beyond the scope of this paper. Thus there would appear to be no advantage to the two-fluid model for quasineutral problems and many advantages for the XMHD model.

2.2. Relaxation model

Eqs. (2.5) and (2.6) are non-dimensionalized to exhibit the dimensionless parameters that characterize the relaxation. This gives the following [28]:

$$\frac{\partial \mathbf{E}}{\partial t} = \frac{c^2}{v^2}(\nabla \times \mathbf{B} - \mathbf{J}) \tag{2.9}$$

$$\frac{\partial \mathbf{J}}{\partial t} + \nabla \cdot \left(\mathbf{u}\mathbf{J} + \mathbf{J}\mathbf{u} - \frac{\lambda_i}{L_0 n}\mathbf{J}\mathbf{J} - \frac{m_i L_0}{m_e \lambda_i}\mathbf{I}P_e \right) = \frac{L_0^2 n}{\lambda_e^2}\left(\mathbf{E} + \mathbf{u} \times \mathbf{B} - \frac{\lambda_i}{L_0 n}\mathbf{J} \times \mathbf{B} - \eta\mathbf{J} \right), \tag{2.10}$$

where $v = L_0/t_0$ is the characteristic speed and L_0, t_0 are representative length and time respectively. The electron and ion inertial lengths are $\lambda_j^2 = m_j/n_0 e^2 \mu_0$. The relaxation parameters are c^2/v^2 and L_0^2/λ_e^2.

In High-Energy-Density (HED) plasmas the phenomena of interest often occur on time scales much slower than the characteristic electron plasma and electron cyclotron frequencies, which means, $v \ll c$ and $\lambda_e \ll L_0$, forcing that (2.9) and (2.10) relax to the equilibrium:

$$\nabla \times \mathbf{B} = \mathbf{J} \tag{2.11}$$

$$\mathbf{E} + \mathbf{u} \times \mathbf{B} - \frac{\lambda_i}{L_0 n}\mathbf{J} \times \mathbf{B} + \frac{\lambda_i}{L_0 n}\nabla P_e = \eta\mathbf{J}. \tag{2.12}$$

This means that, when the electron inertial scale is under-resolved, the solution relaxes to the inertia-less GOL and $\mathbf{J}$ will be constrained by $\mathbf{J} = \nabla \times \mathbf{B}$. This model is implemented into an algorithm in which we use an implicit–explicit time advance, allowing time steps comparable to MHD. Thus we can solve problems in which the Hall effect is important without significant computational cost over that of standard MHD with the caveat that the CFL condition for the speed of light must be respected. Our experience has shown for most problems we can use a much reduced speed of light without affecting the results significantly. Typically this reduction factor is in the range of 15–30 for HED problems. For more information on the relaxation method, please refer to [28].

The formulation of the XMHD model given by (2.1)–(2.7) is not standard [27,30]. The differences are relevant for the implementation of the numerical algorithm. Note that the momentum and energy equations have source terms and as true

source terms they depend only on the independent variables with no derivatives. In most formulations of XMHD the current is a dependent variable determined through Ampére's law and the electric field is determined by the generalized Ohm's law. In the present formulation in which displacement current is retained, the electric field and current density are independent variables having separate evolution equations. Hence the terms on the RHS of (2.2), (2.3), (2.6) and (2.7) are true source terms. There are issues that are potential cause for concern by not having a fully conservative form in which all terms are in divergence form. These are: 1. the $\mathbf{J} \times \mathbf{B}$ force term may affect shock capturing ability of the numerical discretization and 2. the non-positive form of the energy source term could affect the positivity of the pressure. We address the first concern by providing tests that show the DG scheme does well in capturing shocks and discontinuities and the second concern is addressed by proving that the positivity-preserving limiter preserves the stability of the system.

3. Discontinuous Galerkin formulation

In this section, we construct the DG methods that will be used for the XMHD model.

3.1. Local divergence-free discontinuous Galerkin formulation

In this paper, we only consider problems which can be considered invariant in z direction. Therefore, we have $\partial_z = 0$, and $\nabla = (\partial_x, \partial_y, 0)$. Given this, we can summarize Eqs. (2.1)–(2.7) with the following form:

$$\mathbf{U}_t + \mathbf{f}(\mathbf{U})_x + \mathbf{g}(\mathbf{U})_y = \mathbf{s}(\mathbf{U}) \tag{3.1}$$

where

$$\mathbf{U} = (\rho, m_x, m_y, m_z, \mathcal{E}_n, B_x, B_y, B_z, E_x, E_y, E_z, J_x, J_y, J_z, S_e)^T,$$

$$\mathbf{f}(\mathbf{U}) = \Big(m_x, m_x u_x + P, m_y u_x, m_z u_x, (\mathcal{E}_n + P)u_x, 0, -E_z, E_y, 0, c^2 B_z, -c^2 B_y,$$

$$u_x J_x + J_x u_x - \frac{1}{Zne} J_x J_x - \frac{e}{m_e} P_e, u_x J_y + J_x u_y - \frac{1}{Zne} J_x J_y, u_x J_z + J_x u_z - \frac{1}{Zne} J_x J_z, S_e u_{ex} \Big)^T,$$

$$\mathbf{g}(\mathbf{U}) = \Big(m_y, m_x u_y, m_y u_y + P, m_z u_y, (\mathcal{E}_n + P)u_y, E_z, 0, -E_x, -c^2 B_z, 0, c^2 B_x,$$

$$u_y J_x + J_y u_x - \frac{1}{Zne} J_y J_x, u_y J_y + J_y u_y - \frac{1}{Zne} J_y J_y - \frac{e}{m_e} P_e, u_y J_z + J_y u_z - \frac{1}{Zne} J_y J_z, S_e u_{ey} \Big)^T,$$

$$\mathbf{s}(\mathbf{U}) = \Big(0, J_y B_z - J_z B_y, J_z B_x - J_x B_z, J_x B_y - J_y B_x,$$

$$u_x(J_y B_z - J_z B_y) + u_y(J_z B_x - J_x B_z) + u_z(J_x B_y - J_y B_x) + \eta(J_x^2 + J_y^2 + J_z^2),$$

$$0, 0, 0, -\frac{J_x}{\epsilon_0}, -\frac{J_y}{\epsilon_0}, -\frac{J_z}{\epsilon_0}, \frac{Zne^2}{m_e} \Big(E_x + u_y B_z - \frac{1}{Zne} J_y B_z - \eta J_x \Big),$$

$$\frac{Zne^2}{m_e} \Big(E_y + u_z B_x - \frac{1}{Zne} J_z B_x - \eta J_y \Big), \frac{Zne^2}{m_e} \Big(E_z + u_x B_y - \frac{1}{Zne} J_x B_y - \eta J_z \Big),$$

$$(\gamma - 1)n_e^{1-\gamma} \eta(J_x^2 + J_y^2 + J_z^2) \Big)^T \tag{3.2}$$

with

$$u_x = \frac{m_x}{\rho}, \qquad u_y = \frac{m_y}{\rho}, \qquad u_z = \frac{m_z}{\rho},$$

$$u_{xe} = u_x - J_x/(Zen), \qquad u_{ye} = u_y - J_y/(Zen), \qquad u_{ze} = u_z - J_z/(Zen).$$

We consider the computational domain $[0, L_x] \times [0, L_y]$, and use rectangular mesh defined as

$$0 = x_{\frac{1}{2}} < \cdots < x_{N_x + \frac{1}{2}} = L_x, \qquad 0 = y_{\frac{1}{2}} < \cdots < y_{N_y + \frac{1}{2}} = L_y,$$

with $I_{ij} = [x_{i-\frac{1}{2}}, x_{i+\frac{1}{2}}] \times [y_{j-\frac{1}{2}}, y_{j+\frac{1}{2}}]$ representing the cells. For simplicity, we apply uniform meshes only, and denote Δx and Δy to be the mesh sizes in x and y directions, respectively.

Following [23], we define the finite element space as

$$V_h^k = \Big\{ \mathbf{v} : \mathbf{v}|_{I_{ij}} \in \mathbf{P}^k(I_{ij}), \Big(\frac{\partial v_6}{\partial x} + \frac{\partial v_7}{\partial y} \Big) = 0 \Big\},$$

where $\mathbf{P}^k(I_{ij}) = (\mathcal{P}(I_{ij}))^{15}$, with $\mathcal{P}(I_{ij})$ being the space of polynomials of degree at most k in cell I_{ij}. v_6 and v_7 are the sixth and seventh components of the basis functions used to expand B_x and B_y. Note that, by using such a finite element space, $\nabla \cdot \mathbf{B} = 0$ is locally preserved automatically. Although a local divergence free constraint does not guarantee global divergence free solutions, it has been shown that a local condition is very accurate [8], although [1] and [2] report some advantages in using a global divergence free reconstruction over a local constraint. We provide a numerical test of the global divergence of the magnetic field in Section 4.6.2, which supports the conclusion of [8].

Then the DG scheme is the following: find $\mathbf{Q} \in V_h^k$, such that for any $\mathbf{v} \in V_h^k$

$$
\begin{aligned}
(\mathbf{Q}_t, \mathbf{v})_{ij} &= \big(\mathbf{f}(\mathbf{Q}), \mathbf{v}_x\big)_{i,j} + \int_{y_{j-\frac{1}{2}}}^{y_{j+\frac{1}{2}}} \widehat{\mathbf{f}}_{i-\frac{1}{2},j} \mathbf{v}_{i-\frac{1}{2},j}^+ \, dy - \int_{y_{j-\frac{1}{2}}}^{y_{j+\frac{1}{2}}} \widehat{\mathbf{f}}_{i+\frac{1}{2},j} \mathbf{v}_{i+\frac{1}{2},j}^- \, dy \\
&+ \big(\mathbf{g}(\mathbf{Q}), \mathbf{v}_y\big)_{i,j} + \int_{x_{i-\frac{1}{2}}}^{x_{i+\frac{1}{2}}} \widehat{\mathbf{g}}_{i,j-\frac{1}{2}} \mathbf{v}_{i,j-\frac{1}{2}}^+ \, dx - \int_{x_{i-\frac{1}{2}}}^{x_{i+\frac{1}{2}}} \widehat{\mathbf{g}}_{i,j+\frac{1}{2}} \mathbf{v}_{i,j+\frac{1}{2}}^- \, dx \\
&+ \big(\mathbf{s}(\mathbf{Q}), \mathbf{v}\big)_{i,j},
\end{aligned}
\tag{3.3}
$$

where $(\mathbf{u}, \mathbf{v})_{ij} = \int_{I_{ij}} \sum_{\ell=1}^{15} u_\ell v_\ell \, dx \, dy$ and $\mathbf{v}_{i-\frac{1}{2},j}^+(y)$, $\mathbf{v}_{i+\frac{1}{2},j}^-(y)$, $\mathbf{v}_{i,j-\frac{1}{2}}^+(x)$, $\mathbf{v}_{i,j+\frac{1}{2}}^-(x)$ are the traces of $\mathbf{v}$ on left, right, lower, upper edge of the cell I_{ij}, respectively. More details can be found in [42]. With the definition of the traces, the one-dimensional numerical fluxes are: $\widehat{\mathbf{f}}_{i-\frac{1}{2},j} = \widehat{\mathbf{f}}(\mathbf{Q}_{i-\frac{1}{2},j}^-(y), \mathbf{Q}_{i-\frac{1}{2},j}^+(y))$ and $\widehat{\mathbf{g}}_{i,j-\frac{1}{2}} = \widehat{\mathbf{g}}(\mathbf{Q}_{i,j-\frac{1}{2}}^-(x), \mathbf{Q}_{i,j-\frac{1}{2}}^+(x))$. The local Lax–Friedrichs (LLF) flux is used to evaluate $\widehat{\mathbf{f}}_{i-\frac{1}{2},j}$, $\widehat{\mathbf{g}}_{i,j-\frac{1}{2}}$:

$$
\begin{aligned}
\widehat{\mathbf{f}}_{i-\frac{1}{2},j} &= \frac{1}{2}\big[\mathbf{f}(\mathbf{Q}_{i-\frac{1}{2},j}^-(y)) + \mathbf{f}(\mathbf{Q}_{i-\frac{1}{2},j}^+(y))\big] + \frac{1}{2}|\lambda|_{i-\frac{1}{2},j}\big[\mathbf{Q}_{i-\frac{1}{2},j}^-(y) - \mathbf{Q}_{i-\frac{1}{2},j}^+(y)\big] \\
\widehat{\mathbf{g}}_{i,j-\frac{1}{2}} &= \frac{1}{2}\big[\mathbf{g}(\mathbf{Q}_{i,j-\frac{1}{2}}^-(x)) + \mathbf{g}(\mathbf{Q}_{i,j-\frac{1}{2}}^+(x))\big] + \frac{1}{2}|\lambda|_{i,j-\frac{1}{2}}\big[\mathbf{Q}_{i,j-\frac{1}{2}}^-(x) - \mathbf{Q}_{i,j-\frac{1}{2}}^+(x)\big].
\end{aligned}
\tag{3.4}
$$

We do not presently have a solution for a full Riemann solver or even an approximate Riemann solver. Therefore we have used an ad-hoc form of an LLF flux based on an estimate of the maximum eigenvalues of the flux Jacobian computed respectively from the Euler ((2.1)–(2.3)), Maxwell ((2.4)–(2.5)), and GOL ((2.6)–(2.7)) sub-blocks. These maximum eigenvalues, sometimes called freezing speeds [35], are the local values of $|\mathbf{u}| + c_s$, c, $|\mathbf{u}_e| + c_{es}$ for the Euler, Maxwell, and GOL sub-blocks respectively, where $c_{es}^2 = \frac{m_i}{m_e} c_s^2$ is the electron sound speed and $c_s^2 = \gamma P \rho^{-1}$ is the acoustic speed. We have found the LLF flux based on these values to be entirely satisfactory and we note that the same values are used in the finite volume code and that with DG, far less diffusion is exhibited than FV, which will be shown in Section 4.

$|\lambda|_{i,j}$ are the freezing speeds evaluated on cell $\{i, j\}$, and in Eq. (3.4) we set

$$
\begin{aligned}
|\lambda|_{i-\frac{1}{2},j} &= \max\big(|\lambda|_{i-1,j}, |\lambda|_{i,j}\big) \\
|\lambda|_{i,j-\frac{1}{2}} &= \max\big(|\lambda|_{i,j-1}, |\lambda|_{i,j}\big).
\end{aligned}
$$

3.2. Positivity-preserving limiter

Physically, the density ρ and pressure P are positive. Therefore, the exact solution is in a convex set [7]

$$
G = \left\{ \mathbf{w} = \begin{pmatrix} \rho \\ m_x \\ m_y \\ m_z \\ \mathcal{E}_n \\ S_e \end{pmatrix} \,\middle|\, \rho > 0 \text{ and } P = (\gamma - 1)\left(\mathcal{E}_n - \frac{1}{2}(m_x^2 + m_y^2 + m_z^2)/\rho\right) > 0 \text{ and } S_e > 0 \right\}.
\tag{3.5}
$$

We want to construct the numerical solution which is also in the set (3.5). We use forward Euler for time integration and maintain the positivity of density, pressure and electron entropy density at time level $n + 1$, provided that they are positive at time level n. It is clear that, $\mathcal{E}_n > 0$ is automatically established if we have $\rho > 0$ and $P > 0$. In this section, we prove that the positivity-preserving property can be guaranteed with a special limiter in our XMHD model.

We consider the first five equations and the last one in the system (3.3). Following [42], at time level n, we use a vector of polynomials of degree k, $\mathbf{w}_{ij}^n = (\rho_{ij}^n, m_{xij}^n, m_{yij}^n, m_{zij}^n, \mathcal{E}_{nij}^n, S_{eij}^n)$ to approximate the exact solution, and define the cell average $\overline{\mathbf{w}}_{ij}^n = (\overline{\rho}_{ij}^n, \overline{m}_{xij}^n, \overline{m}_{yij}^n, \overline{m}_{zij}^n, \overline{\mathcal{E}}_{nij}^n, \overline{S}_e)$. In this section, we always use $\mathbf{u}_{ij}^n = (u_{xij}^n, u_{yij}^n, u_{zij}^n)^T$ for $\frac{\mathbf{m}_{ij}^n}{\rho_{ij}^n} = \left(\frac{m_{xij}^n}{\rho_{ij}^n}, \frac{m_{yij}^n}{\rho_{ij}^n}, \frac{m_{zij}^n}{\rho_{ij}^n}\right)^T$

as the numerical velocity in cell I_{ij} at time level n. For simplicity, if we consider a generic numerical solution on the whole computational domain, then the subscript ij will be omitted. By taking the test function $\mathbf{v} = 1$ in (3.3) we have the scheme satisfied by the cell averages

$$\overline{\mathbf{w}}_{ij}^{n+1} = \frac{1}{2}\mathbf{H}_1 + \frac{1}{2}\mathbf{H}_2, \tag{3.6}$$

where

$$\mathbf{H}_1 = \overline{\mathbf{w}}_{ij}^n + \frac{2\Delta t}{\Delta x \Delta y} \int\limits_{y_{j-\frac{1}{2}}}^{y_{j+\frac{1}{2}}} \hat{\mathbf{f}}\big(\mathbf{w}_{i-\frac{1}{2},j}^-(y), \mathbf{w}_{i-\frac{1}{2},j}^+(y)\big) - \hat{\mathbf{f}}\big(\mathbf{w}_{i+\frac{1}{2},j}^-(y), \mathbf{w}_{i+\frac{1}{2},j}^+(y)\big)dy$$

$$+ \frac{2\Delta t}{\Delta x \Delta y} \int\limits_{x_{i-\frac{1}{2}}}^{x_{i+\frac{1}{2}}} \hat{\mathbf{g}}\big(\mathbf{w}_{i,j-\frac{1}{2}}^-(x), \mathbf{w}_{i,j-\frac{1}{2}}^+(x)\big) - \hat{\mathbf{g}}\big(\mathbf{w}_{i,j+\frac{1}{2}}^-(x), \mathbf{w}_{i,j+\frac{1}{2}}^+(x)\big)dx \tag{3.7}$$

$$\mathbf{H}_2 = \overline{\mathbf{w}}_{ij}^n + \frac{2\Delta t}{\Delta x \Delta y} \int\limits_{I_{ij}} \mathbf{s}(x, y)dxdy, \tag{3.8}$$

with $\hat{\mathbf{f}}(\cdot, \cdot)$ and $\hat{\mathbf{g}}(\cdot, \cdot)$ being the one-dimensional numerical fluxes and

$$\mathbf{s} = \big(0, \mathbf{J} \times \mathbf{B}, \mathbf{u} \cdot (\mathbf{J} \times \mathbf{B}) + \eta \mathbf{J}^2, (\gamma - 1)n_e^{1-\gamma}\eta\mathbf{J}^2\big)^T.$$

For accuracy, we use L-point Gauss quadratures with $L \geq k + 1$ to approximate the integral in (3.7). We refer the readers to [11] for more details of this requirement. The Gauss quadrature points on $[x_{i-\frac{1}{2}}, x_{i+\frac{1}{2}}]$ and $[y_{j-\frac{1}{2}}, y_{j+\frac{1}{2}}]$ are denoted by

$$p_i^x = \{x_i^\beta : \beta = 1, \cdots, L\} \quad \text{and} \quad p_j^y = \{y_j^\beta : \beta = 1, \cdots, L\},$$

respectively. Also, we denote ω_β as the corresponding weights on the interval $[-1, 1]$. Then the Gauss quadrature formula on the interval $[x_{i-\frac{1}{2}}, x_{i+\frac{1}{2}}]$ can be written as

$$\int\limits_{x_{i-\frac{1}{2}}}^{x_{i+\frac{1}{2}}} f(x)dx \approx \sum_{\beta=1}^{L} \omega_\beta f\big(x_i^\beta\big)h_i/2,$$

where $h_i = x_{i+\frac{1}{2}} - x_{i-\frac{1}{2}}$. Moreover, we use

$$\hat{p}_i^x = \{\hat{x}_i^\alpha : \alpha = 0, \cdots, M\} \quad \text{and} \quad \hat{p}_j^y = \{\hat{y}_j^\alpha : \alpha = 0, \cdots, M\}$$

with $2M - 1 \geq k$, as the Gauss–Lobatto points on $[x_{i-\frac{1}{2}}, x_{i+\frac{1}{2}}]$ and $[y_{j-\frac{1}{2}}, y_{j+\frac{1}{2}}]$, respectively. Also, we denote $\hat{\omega}_\alpha$ as the corresponding weights on the interval $[-1, 1]$. Then the Gauss–Lobatto quadrature formula on the interval $[x_{i-\frac{1}{2}}, x_{i+\frac{1}{2}}]$ can be written as

$$\int\limits_{x_{i-\frac{1}{2}}}^{x_{i+\frac{1}{2}}} f(x)dx \approx \sum_{\alpha=0}^{M} \hat{\omega}_\alpha f\big(\hat{x}_i^\alpha\big)h_i/2.$$

Let $\lambda_1 = \frac{\Delta t}{\Delta x}$ and $\lambda_2 = \frac{\Delta t}{\Delta y}$, then $\mathbf{H}_1$ becomes

$$\mathbf{H}_1 = \overline{\mathbf{w}}_{ij}^n + 2\lambda_1 \sum_{\beta=1}^{L} \omega_\beta\big[\hat{\mathbf{f}}\big(\mathbf{w}_{i-\frac{1}{2},\beta}^-, \mathbf{w}_{i-\frac{1}{2},\beta}^+\big) - \hat{\mathbf{f}}\big(\mathbf{w}_{i+\frac{1}{2},\beta}^-, \mathbf{w}_{i+\frac{1}{2},\beta}^+\big)\big]$$

$$+ 2\lambda_2 \sum_{\beta=1}^{L} \omega_\beta\big[\hat{\mathbf{g}}\big(\mathbf{w}_{\beta,j-\frac{1}{2}}^-, \mathbf{w}_{\beta,j-\frac{1}{2}}^+\big) - \hat{\mathbf{g}}\big(\mathbf{w}_{\beta,j+\frac{1}{2}}^-, \mathbf{w}_{\beta,j+\frac{1}{2}}^+\big)\big], \tag{3.9}$$

where $\mathbf{w}_{i-\frac{1}{2},\beta}^- = \mathbf{w}_{i-\frac{1}{2},j}^-(y_j^\beta)$ is a point value in the Gauss quadrature. Likewise for the other point values. Then we have the following lemma

Lemma 3.1. *For the discontinuous Galerkin method with the LLF flux, if* $\mathbf{w^n} \in G$, *then* $\mathbf{H}_1 \in G$ *under the CFL condition*

$$\frac{\Delta t}{\Delta x} \max\big(\|u_x + C_0\|_\infty, \|u_y\|_\infty, \|u_z\|_\infty\big) + \frac{\Delta t}{\Delta y} \max\big(\|u_x\|_\infty, \|u_y + C_0\|_\infty, \|u_z\|_\infty\big) \le \frac{\hat{\omega}_0}{2}, \tag{3.10}$$

and

$$\frac{\Delta t}{\Delta x} \max\big(\|(u_e)_x\|_\infty\big) + \frac{\Delta t}{\Delta y} \max\big(\|(u_e)_y\|_\infty\big) \le \frac{\hat{\omega}_0}{2}, \tag{3.11}$$

where $C_0 = \sqrt{\frac{\gamma P}{\rho}}$, $\|v\|_\infty$ *is the standard* L^∞-*norm of* v *on the whole computational domain, and* $(u_e)_x$ *and* $(u_e)_y$ *are the* x *and* y *components of* $\mathbf{u_e}$.

Proof. The proof follows from [42] with some minor changes, so we omit it. □

Now we consider the source term $\mathbf{s}$. We use a Gauss quadrature with L points to compute the integral of the source. Then $\mathbf{H}_2$ becomes

$$\mathbf{H}_2 = \sum_{\alpha=1}^{L} \sum_{\beta=1}^{L} \omega_\alpha \omega_\beta \mathbf{h}_{\alpha\beta},$$

where

$$\mathbf{h}_{\alpha\beta} = \mathbf{w}_{\alpha\beta}^n + 2\Delta t \mathbf{s}_{\alpha\beta}$$

and $\mathbf{w}_{\alpha\beta}^n$ denotes the point value of $\mathbf{w}_{ij}^n$ at (x_i^α, y_j^β). Likewise for $\mathbf{s}_{\alpha\beta}$.

Lemma 3.2. *Suppose* $\mathbf{w}^n \in G$, *then we have* $\mathbf{h}_{\alpha\beta} \in G$ *under the condition*

$$\Delta t \le \min_{i,j,\alpha,\beta} A_s\big(x_i^\alpha, y_j^\beta\big), \tag{3.12}$$

where

$$A_s = \frac{\eta \mathbf{J}^2 \rho + \sqrt{\eta^2 \mathbf{J}^4 \rho^2 + 2P(\mathbf{J} \times \mathbf{B})^2 \rho/(\gamma - 1)}}{2(\mathbf{J} \times \mathbf{B})^2}.$$

Proof. Suppose $\mathbf{h}_{\alpha\beta} = (\check{\rho}, \rho\check{\mathbf{u}}, \check{\mathcal{E}}_n, \check{S}_e)^T$, with $\check{\mathbf{u}} = \frac{\check{\mathbf{m}}}{\check{\rho}}$. For simplicity, in this lemma, if we consider the point value at (x_i^α, y_j^β) at time level n, the corresponding index will be omitted. Then it is easy to show that $\check{\rho} = \rho^n > 0$ and $\check{S}_e > 0$. The second inequality is due to the positivity of the source term in (2.7). So we only need to show $\check{P} = (\gamma - 1)(\check{\mathcal{E}}_n - \frac{1}{2}\check{\rho}\check{\mathbf{u}}^2) > 0$. Clearly, we have:

$$\check{\mathbf{m}} = \mathbf{m} + 2\Delta t(\mathbf{J} \times \mathbf{B})$$

$$\check{\mathcal{E}}_n = \mathcal{E}_n + 2\Delta t\big(\mathbf{u} \cdot (\mathbf{J} \times \mathbf{B}) + \eta \mathbf{J}^2\big)$$

which further yields

$$\frac{\check{P}}{\gamma - 1} = \mathcal{E}_n + 2\Delta t\big(\mathbf{u} \cdot (\mathbf{J} \times \mathbf{B}) + \eta \mathbf{J}^2\big) - \frac{[\mathbf{m} + 2\Delta t(\mathbf{J} \times \mathbf{B})]^2}{2\rho}$$

$$= \frac{P}{\gamma - 1} + 2\Delta t \eta \mathbf{J}^2 - 2\Delta t^2 \frac{(\mathbf{J} \times \mathbf{B})^2}{\rho}.$$

Therefore, $\check{P} > 0$ provided

$$\Delta t \le \frac{\eta \mathbf{J}^2 \rho + \sqrt{\eta^2 \mathbf{J}^4 \rho^2 + 2P(\mathbf{J} \times \mathbf{B})^2 \rho/(\gamma - 1)}}{2(\mathbf{J} \times \mathbf{B})^2}.$$

This condition can be made physically transparent as follows:

$$\Delta t < \frac{1}{\sqrt{2(\gamma - 1)}} \frac{v_{th}}{v_A v_A'} \quad \text{or} \quad \Delta t < \frac{\eta}{\mu_0} \frac{1}{v_A^2}$$

is sufficient for $\check{P} > 0$, where v_{th} is the thermal speed, v_A is the Alfvén speed, $v_A' \equiv \frac{\nabla \times \mathbf{B}}{\sqrt{\mu_0 n m_i}}$. □

Noticing the fact that $\mathbf{w}^{n+1}$ is the convex combination of $\mathbf{H}_1$ and $\mathbf{h}_{\alpha\beta}$ we have the following result.

Theorem 3.1. *Consider the scheme satisfied by the cell averages of a DG formulation* (3.6) *with Lax–Friedrichs flux, if* $\mathbf{w}^n(\widehat{x}_i^\alpha, y_j^\beta)$, $\mathbf{w}^n(x_i^\alpha, \widehat{y}_j^\beta)$, $\mathbf{w}^n(x_i^\alpha, y_j^\beta) \in G$, *then* $\overline{\mathbf{w}}^{n+1} \in G$ *under the CFL condition* (3.10) *and* (3.12).

Remark 3.1. Since MHD model shares the first five equations with XMHD model in system (3.3), the proof that the positivity-preserving property can be guaranteed in MHD model follows exactly the same process, so we omit it here.

Remark 3.2. We have shown that the positivity-preserving property of pressure in the Euler equations extends to the XMHD model or MHD model. As indicated by (3.12), in extreme cases where the resistivity η is zero, and pressure P is very small, we may not be able to find a reasonable Δt to preserve the positivity of $\check{P}$. Apparently that is an exceptional situation, which we have not yet encountered.

Now, we provide the implementation of the algorithm.

- Choose a small number consistent with the density that can be viewed as vacuum, which is typically $\varepsilon = 10^{-9}$.
- If $\overline{\rho}_{ij}^n > \varepsilon$, then proceed to the following steps. Otherwise, ρ_{ij}^n is identified as the approximation to vacuum, and we take $\mathbf{w}_{ij}^n = \overline{\mathbf{w}}_{ij}^n$ as the numerical solution and skip the following steps.
- In each cell, modify the density first. Evaluate

$$\rho_{\min} = \min_{\alpha\beta}\{\rho_{ij}^n(\widehat{x}_i^\alpha, y_j^\beta), \rho_{ij}^n(x_i^\alpha, \widehat{y}_j^\beta), \rho_{ij}^n(x_i^\alpha, y_j^\beta)\}.$$

If $\rho_{\min} < \varepsilon$, then take $\widetilde{\rho}_{ij}^n$ as

$$\widetilde{\rho}_{ij}^n = \overline{\rho}_{ij}^n + \theta_{ij}^n(\rho_{ij}^n - \overline{\rho}_{ij}^n),$$

with

$$\theta_{ij}^n = \frac{\overline{\rho}_{ij}^n - \varepsilon}{\overline{\rho}_{ij}^n - \rho_{\min}},$$

and use $\widetilde{\rho}_{ij}^n$ as the new numerical density by assigning: $\rho_{ij}^n = \widetilde{\rho}_{ij}^n$

- Modify the S_e. Evaluate

$$S_{e\min} = \min_{\alpha\beta}\{S_{eij}^n(\widehat{x}_i^\alpha, y_j^\beta), S_{eij}^n(x_i^\alpha, \widehat{y}_j^\beta), S_{eij}^n(x_i^\alpha, y_j^\beta)\}.$$

If $S_{e\min} < \varepsilon$, then take $\widetilde{S}_{eij}^n$ as

$$\widetilde{S}_{eij}^n = \overline{S}_{eij}^n + \theta_{ij}^n(S_{eij}^n - \overline{S}_{eij}^n),$$

with

$$\theta_{ij}^n = \frac{\overline{S}_{eij}^n - \varepsilon}{\overline{S}_{eij}^n - S_{e\min}},$$

and use $\widetilde{S}_{eij}^n$ as the new electron entropy density by assigning: $S_{eij}^n = \widetilde{S}_{eij}^n$

- Modify the pressure: For each $\mathbf{q} \in \{\mathbf{w}(\widehat{x}_i^\alpha, y_j^\beta), \mathbf{w}(x_i^\alpha, \widehat{y}_j^\beta), \mathbf{w}(x_i^\alpha, y_j^\beta)\}$, compute $P(\mathbf{q})$. If $P(\mathbf{q}) \geq \varepsilon$, then we take $s_{\mathbf{q}} = 1$. Otherwise, we calculate $s_{\mathbf{q}}$ such that

$$P\big((1 - s_{\mathbf{q}})\overline{\mathbf{w}}_{\mathbf{q}} + s_{\mathbf{q}}\mathbf{q}\big) = \varepsilon.$$

Modify $\widetilde{\mathbf{w}}_{ij}^n = \overline{\mathbf{w}}_{ij}^n + \theta(\mathbf{w}_{ij}^n - \overline{\mathbf{w}}_{ij}^n)$ with $\theta = \min_{\mathbf{q}}\{s_{\mathbf{q}}\}$.

- Use $\widetilde{\mathbf{w}}_{ij}^n$ as the DG approximation.

3.3. Time integration schemes

As described in [26,28], we use a semi-implicit advance scheme for the stiff source terms in (2.10) and (2.9). The split level implicit–explicit time advance is performed as follows:

1. Use 2nd order Runge–Kutta (Heun) method to perform time advance for (2.1)–(2.4) and (2.7)
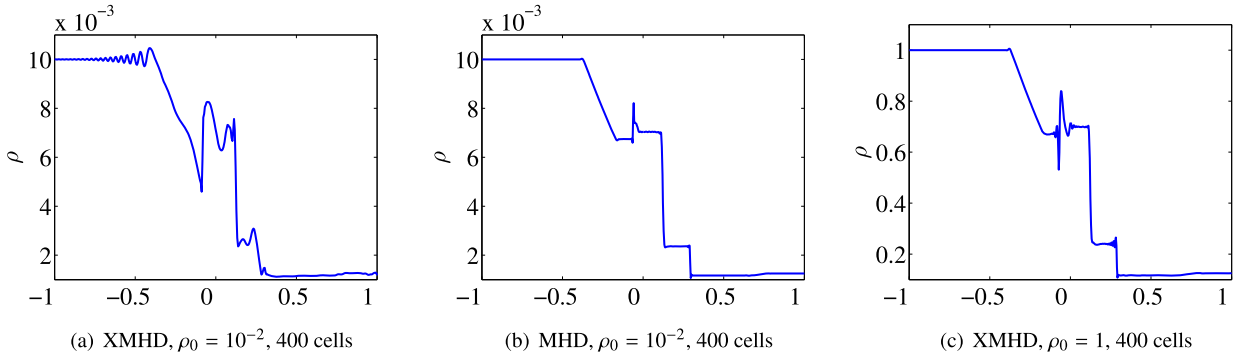
Fig. 1. Brio–Wu shock tube test. Density as a function of position, captured at $t = 2.1 \times 10^{-2}$.

2. Use 2nd order Runge–Kutta method to perform time advance for flux part in (2.9)–(2.10):

$$\frac{\partial \mathbf{E}}{\partial t} = \frac{c^2}{v^2}(\nabla \times \mathbf{B}) \tag{3.13}$$

$$\frac{\partial \mathbf{J}}{\partial t} + \nabla \cdot \left(\mathbf{uJ} + \mathbf{Ju} - \frac{\lambda_i}{L_0 n}\mathbf{JJ} - \frac{m_i}{m_e}\frac{L_0}{\lambda_i}\mathbf{I}P_e \right) = 0 \tag{3.14}$$

3. Save the updated values obtained from step 1 and 2 as Q^*.
4. Perform a semi-implicit time advance for the source terms in (2.9)–(2.10). This leads to the following spatially local linear algebraic equations for $\mathbf{E}^{n+1}$ and $\mathbf{J}^{n+1}$

$$\mathbf{E}^{n+1} = \mathbf{E}^* - \Delta t \frac{c^2}{v^2}\mathbf{J}^{n+1} \tag{3.15}$$

$$\mathbf{J}^{n+1} = \mathbf{J}^* + \Delta t \frac{L_0^2 n^*}{\lambda_e^2} \left(\mathbf{E}^{n+1} + \mathbf{u}^* \times \mathbf{B}^* - \frac{\lambda_i}{L_0 n^*}\mathbf{J}^{n+1} \times \mathbf{B}^* - \eta^*\mathbf{J}^{n+1} \right). \tag{3.16}$$

The semi-implicit step is performed after each step of the explicit Runge–Kutta time advance of (3.13) and (3.14). This time advance method forces a relaxation solution to (2.11) and (2.12) in the relaxation limit and accurately computes the current even if the relaxation limit is not approached, that is, when the electron inertial length scale is resolved [28]. The time advance could also be performed using a higher order strong-stability preserving integrator such as the third order Shu–Osher Runge–Kutta method [33].

4. Numerical tests

In this section, we present numerical examples to demonstrate the advantages of positivity-preserving DG scheme. For all the examples, if not otherwise stated, we use a 2nd order DG scheme.

For the tests done in Sections 4.1–4.3, we non-dimensionalize (2.1)–(2.7) as follows: $\mathbf{U} = U_0\tilde{\mathbf{U}}$, where $\tilde{\mathbf{U}}$ is the set of dimensionless variables and U_0 is the set of dimensional normalization factors. For U_0 we used $n_0 = 6 \times 10^{28}$ m^{-3}, $t_0 = 100$ ns, $L_0 = 1$ mm, $v_0 = 10^4$ m s^{-1}, $B_0 = 580$ T, $E_0 = 5.8 \times 10^6$ V/m, $J_0 = 4.6 \times 10^{11}$ A/m^2, $T_0 = 28$ eV, $\eta_0 = 1.3 \times 10^{-5}$ Ω m, and the ion mass number is taken to be 27 for Aluminum.

4.1. The Brio–Wu shock tube problem

We first test the code against the benchmark problem originally used by Brio and Wu [5]. We employ the initial condition:

$$(\rho, u_x, u_y, u_z, P, P_e, B_x, B_y, B_z) = \begin{cases} (1.000\rho_0, 0, 0, 0, 1.0\rho_0, 0.50\rho_0, 0.75\sqrt{\rho_0}, +\sqrt{\rho_0}, 0) & \text{for } x < 0 \\ (0.125\rho_0, 0, 0, 0, 0.1\rho_0, 0.05\rho_0, 0.75\sqrt{\rho_0}, -\sqrt{\rho_0}, 0) & \text{for } x > 0 \end{cases}$$

$$(E_x, E_y, E_z, J_x, J_y, J_z) = (0, 0, 0, 0, 0, 0).$$

When $\rho_0 = 10^{-2}$, with a resolution of 400, we have $\frac{\lambda_e}{\Delta x} = 4.34 \times 10^{-2}$ and $\frac{\lambda_i}{\Delta x} = 1.9$, so the ion inertial length λ_i is resolved by the spatial grid Δx, and the Hall term in (2.10) becomes important; The Hall term allows for decoupling of the ion motion from the electron flow into which the magnetic field is frozen. The Hall effect introduces dispersive whistler wave, which becomes the fastest wave in the system producing oscillations seen in Fig. 1(a), which is distinctly different from MHD [5], but similar to the two-fluid results [25].

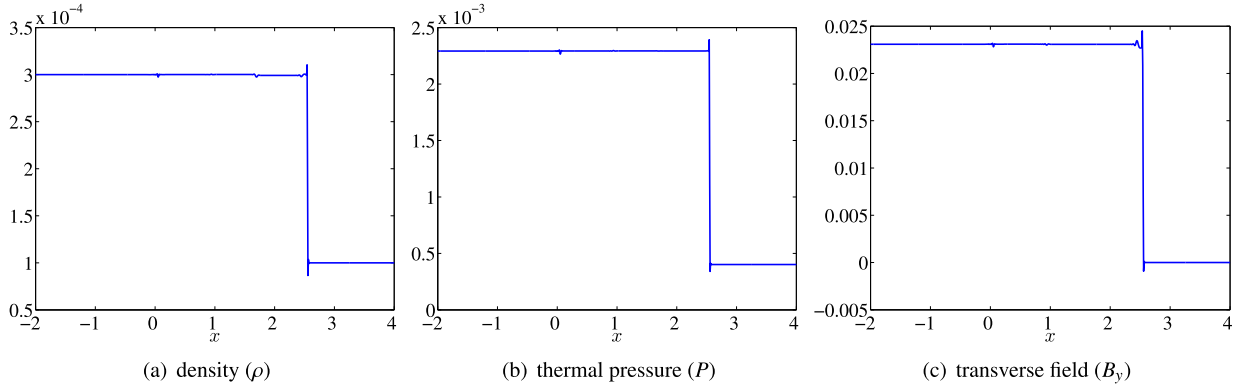For comparison, the MHD result is presented in Fig. 1(b), the model used is ideal-MHD model.

Fig. 2. Density, thermal pressure and transverse field in a fast switch-on shock with ideal-MHD model, 400 cells, initial shock position at $x = 0$.
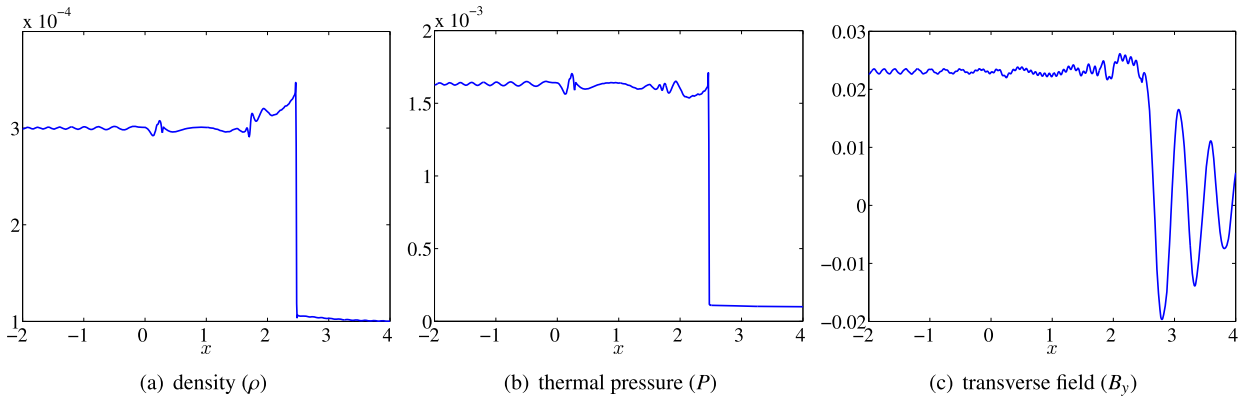

Fig. 3. Density, thermal pressure and transverse field in a fast switch-on shock with XMHD model, 400 cells, initial shock position at $x = 0$.

When the density is increased to $\rho_0 = 1$, with a resolution of 400, we have $\frac{\lambda_e}{\Delta x} = 4.34 \times 10^{-3}$ and $\frac{\lambda_i}{\Delta x} = 0.19$, consequently λ_i is not resolved by the spatial grid size, thus the result, as shown in Fig. 1(c), becomes close to the MHD result in [5].

In this test, the flow is always outgoing on the boundaries, and we use an outflow boundary condition. However, when $\rho_0 = 10^{-2}$, oscillating waves are introduced, causing the flow direction on the boundary to oscillate. We have to use inflow boundary condition when the flow becomes inward.

4.2. Fast shock test

The MHD fast shock is not included in the Brio–Wu problem. Therefore we provide a test by following the fast shock initial conditions in [13], with minor modifications. This test shows that the scheme correctly captures the shock even though the magnetic force is represented by the $\mathbf{J} \times \mathbf{B}$ source term and is not in full conservation form.

The initial state is as follows:

$$(\rho, u_x, u_y, u_z, P, P_e, B_x, B_y, B_z) = \begin{cases} (3\rho_0, 3.444, -1.333, 0, 16.33\rho_0, 8.16\rho_0, 3\sqrt{\rho_0}, 2.309\sqrt{\rho_0}, 0) & \text{for } x < 0 \\ (1\rho_0, 0.000, +0.000, 0, 1.000\rho_0, 0.50\rho_0, 3\sqrt{\rho_0}, 0.000\sqrt{\rho_0}, 0) & \text{for } x > 0 \end{cases}$$

$$(E_x, E_y, E_z, J_x, J_y, J_z) = (0, 0, 0, 0, 0, 0).$$

We set $\rho_0 = 10^{-4}$, with a resolution of $\lambda_e/\Delta x = 0.144$ and $\lambda_i/\Delta x = 6.3$. Fig. 2 shows the ideal-MHD results, note that the shock structure is preserved very well, with only 1 grid cell in the shock. There are small oscillations near the shock region, which are expected since positivity-preserving limiter (PP-limiter) is the only limiter used in this scheme, which does not smooth away oscillations as much as a TVD limiter does. The use of slope limiter [18] can remove all the oscillations. No noticeable difference is found using a finer mesh, which implies the scheme is converged with a resolution as low as 400. Numerical result gives an average shock speed as 5.14, while its analytical solution is 5.17, taken into consideration the measurement error, the results are very close.

With XMHD model, we obtain results shown in Fig. 3. As there are no steady-state shock solutions in the XMHD model, the discontinuity emit waves that propagate outwards. The fact that there is a component of $\mathbf{B}$, i.e., B_x, parallel to the
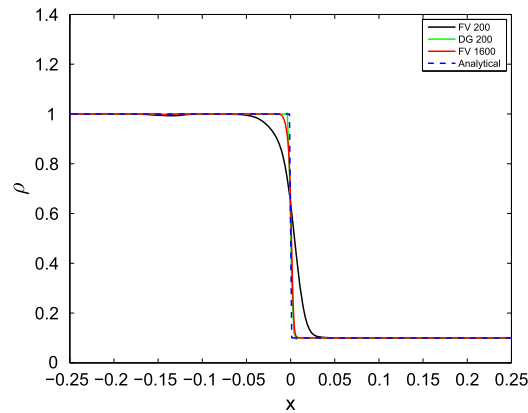
Fig. 4. DG vs. FV result for Pressure Balance Test. FV with 200 cells is most diffusive shown in black, DG with 200 cells shown in green agrees with analytical results best; FV with 1600 cells shown in red is closer to analytical results but still not as good as DG results with 200 cells. (For interpretation of the references to color in this figure legend, the reader is referred to the web version of this article.)

wave vector **k** and no pressure or density perturbations suggests that whistler waves are emitted and cause the oscillations observed in the B_y plot in Fig. 3(c).

4.3. Pressure balance test

Here we provide a test [32] which more directly shows that DG is much less diffusive than second order FV and which shows the necessity of the PP-limiter. We set up the test with the following initial condition to guarantee the initial pressure balance:

$$(\rho, P, P_e, u_x, u_y, u_z, B_x, B_y, B_z, J_x, J_y, J_z) = \begin{cases} (1.0, 100., 50, 0, 0, 0, 0, 10.0000, 0, 0, 0, 0) & \text{for } x < 0 \\ (0.1, 10.0, 5., 0, 0, 0, 0, 16.7332, 0, 0, 0, 0) & \text{for } x > 0 \end{cases}$$

$$(E_x, E_y, E_z, J_x, J_y, J_z) = (0, 0, 0, 0, 0, 0).$$

We did this test with ideal-MHD model. The resistivity is set to zero leaving numerical diffusion as the only potential cause for plasma or magnetic flux to diffuse. In this way one can directly tell how diffusive a scheme is by observing the amount of diffusion. The result is as shown in Fig. 4, from which we can see that, with the same resolution (200), FV result is far more diffusive than DG. We find that FV needs 8 times the resolution (1600) to be comparable to DG with a resolution of 200. And FV takes 200 times longer than DG for producing comparable results.

4.4. Moving planar foil

For problems with solutions containing δ-singularities most numerical methods perform poorly, since many numerical techniques approach these problems by modifying them with smooth kernels, and the singularities are severely smeared as a result. However, DG methods are based on the weak formulation, hence can solve such problems without modifications, leading to a very accurate result [38]. Here, we demonstrate this advantage by doing a moving planar aluminum foil problem with XMHD model. The planar foil, being sufficiently thin compared to our system, can be viewed as a δ-function. A magnetic field **B** is applied parallel to the foil, producing a current **J** flowing perpendicular to the direction of the applied magnetic field. As a result, a $\mathbf{J} \times \mathbf{B}$ force is produced perpendicular to the surface of the foil, accelerating it to the right. In the simulation, the foil is 6.25 μm (one grid cell) thick, 10 mm wide, magnitude of **B** is 116 T. Figs. 5(a)–5(c) are line plots captured at $t = 34$ ns by viewing in the direction parallel to the foil. Fig. 5(a) shows the DG result with 1600 mesh points. The δ structure is well preserved, the widest part spans only about 3 cells. Taking into account the thermal expansion, the widening because of numerical diffusion is small. However, for FV, also with 1600 mesh points, shown in Fig. 5(b), the foil expands much more. When FV mesh is refined to 11 200 cells, the result in Fig. 5(c) is much closer to DG in Fig. 5(a).

It is worth pointing out that this problem spans 9 orders of magnitude in density range, which covers near-vacuum (10^{19} m^{-3}) to solid density (10^{28} m^{-3}). That means, although a PP-limiter does not smooth oscillations near discontinuities as much as a TVD limiter does, it does preserve the stability of a system with a large dynamic range and steep density gradients. If the PP-limiter is turned off the results are very unstable and the test fails in a few time steps.

4.5. Some remarks on the comparison between DG and FV

From the tests done in Sections 4.3 and 4.4, and from some other tests we summarize our observations. The FV tests here are done with an implicit–explicit MUSCL scheme (Monotone Upwind Scheme for Conservation Laws) [14,22,36], using a TVD limiter (van Leer limiter). We did not use PP-limiter for the FV scheme because a PP-limiter restrict the Courant
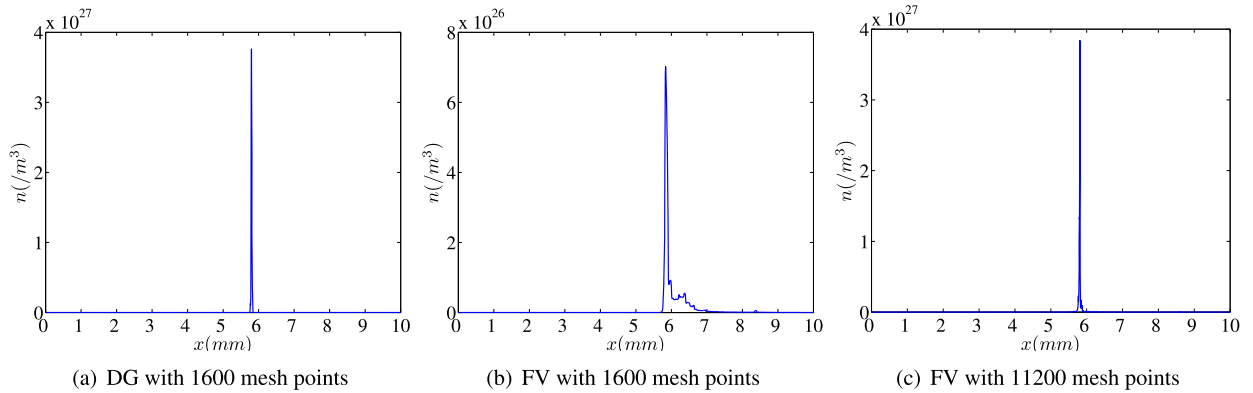
(a) DG with 1600 mesh points (b) FV with 1600 mesh points (c) FV with 11200 mesh points

Fig. 5. Number density n as a function of position x captured at $t = 34$ ns; Initial foil position: $x = 5$ mm.

number to about 0.2, while with a TVD FV scheme we can use a Courant number up to 0.6, thus PP-limiter increases the CPU time by a factor of three. We decided that it was not worth implementing a PP-limiter for our FV test results, which we will further verify through future work. On the other hand, a TVD DG scheme also requires a Courant number around 0.2, thus there is no additional computational expense for DG to obtain the second order accuracy guaranteed by PP-limiter.

From all problems we have tested DG performs better than FV, as determined by less time and memory for producing comparable results. But the quantitative comparison is problem-dependent. For certain kinds of problems, e.g., shock problem and problems with a density profile as a δ function or with a steep gradient, as shown in Sections 4.3 and 4.4, DG performs much better than FV by using a computation time orders of magnitude less. For other problems, FV usually takes 3–4 times larger resolution to achieve the same result as DG, and takes 2–6 times longer to run. The reason for the better performance is that DG scheme is more compact and stores more localized information, so that it resolves the boundary layers and detailed local structures better, while FV uses a more extended stencil, which makes it easier for local information to diffuse away.

### 4.6. Two-dimensional tests and comparison of XMHD to MHD

We provide two additional tests that demonstrate the two-dimensional capabilities of the method and further highlight the differences between XMHD and MHD. The first test is a two dimensional shock problem which requires demanding performance on the shock capturing ability of the algorithm and which illustrates how the Hall term can greatly affect the results when compared to MHD. It also shows that the semi-implicit method allows computation of the Hall effect using a much reduced time step than would be required for a fully explicit computation. The second test is a collisionless reconnection test following the GEM challenge [4] tests. The purpose of this test is to display the method's capabilities in the parameter regime where electron inertia plays a fundamental physical role.

4.6.1. Collisional bow-shock problem

The problem is set up as follows: The domain is $x \in (-20.0 \text{ mm}, 13.0 \text{ mm})$, $y \in (-20.0 \text{ mm}, 20.0 \text{ mm})$; 400 cells are used in y direction, while 330 cells for the x direction. The whole domain is initialized with uniform number density as $n = 10^{23}$ m^{-3}, temperature as 14 eV, magnetic field as $B_y = 16.4$ T. We use Aluminum as the plasma material. And use spitzer resistivity for η. Inflow from left boundary with velocity as $u_x = 200$ km s^{-1}, sonic Mach number as $M_s = 17$, Alfvénic Mach number as $M_a = 2.24$ and magnetosonic Mach number as $M_f = 2.22$. In the region, we put a block of size 0.6 mm $\times$ 0.6 mm with its center 14 mm from left boundary, 20 mm from lower boundary. The block is constructed as a boundary condition on the block's 4 edges ensuring that the mass flux normal to every edge is zero.

The test is done with MHD model and XMHD models separately, and the results at $t = 140$ ns are shown in Figs. 6(a) and 6(b). With the inflow being super-magnetosonic, a magnetosonic shock (fast shock in this case) will appear, as shown in both figures. But the shapes are considerably different using these two models. The differences are due to the Hall term in XMHD in the region behind the block. In this low-density region the Hall term suppresses current flow thereby affecting the magnetic field. While in MHD, without a vacuum resistivity, there is no such a suppression, allowing the current to grow unphysically large. The unphysical current forms a current sheet that is sufficient to support an X-point behind the block, then the plasma and magnetic flux piling up in front of the block gets through by reconnection. This mechanism for flux transport is mitigated by the Hall term in XMHD under the conditions we have chosen for this test, thereby producing very different results. If density is increased so that the Hall term is rendered ineffective, we find that XMHD results approach MHD results.

We point out that the PP-limiter is essential for this test. When it is turned off a low pressure dip immediately forms behind the block and evolves to eventually become negative. We also point out that, we use the same time step for XMHD simulation with an MHD simulation, which saves considerable computational cost as compared to a fully explicit algorithm.
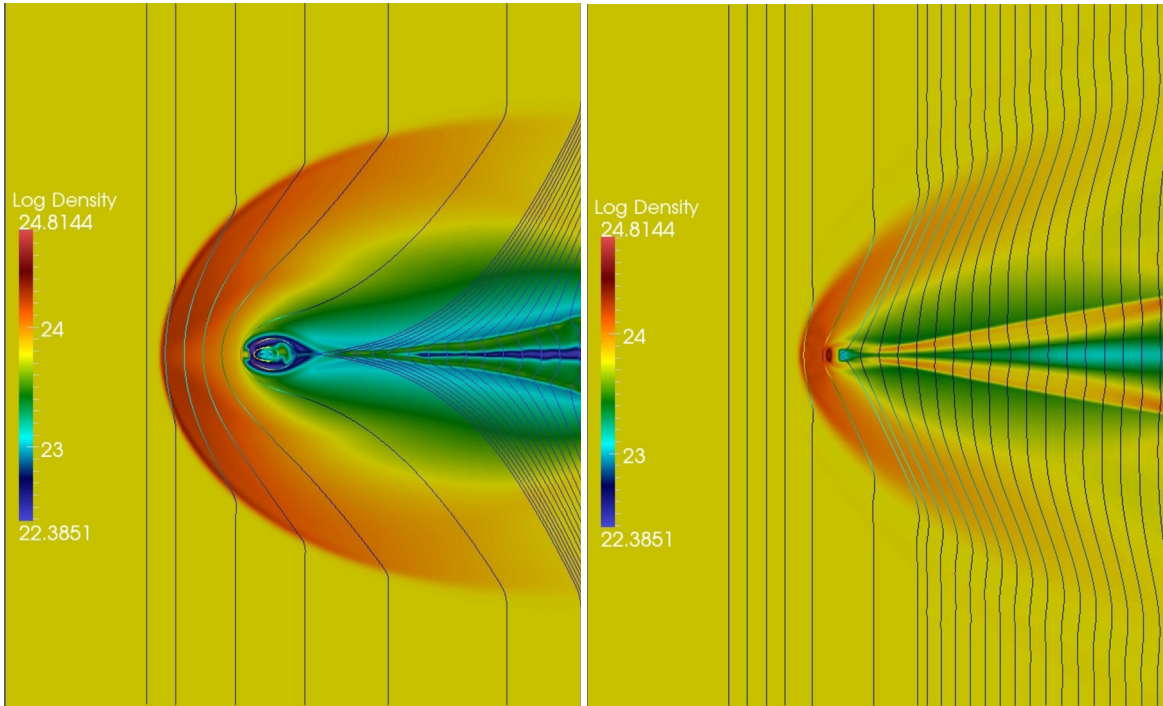
(a) Magnetic field lines with a background color plot log(n) with MHD

(b) Magnetic field lines with a background color plot log(n) with XMHD

Fig. 6. Bow shock simulation, captured at $t = 140$ ns.

It is important to note that the MHD results can be made to agree much better with XMHD by employing a suitable vacuum resistivity to suppress the current in low density region. However, one does not know *a priori* the spatial form or value needed for the vacuum resistivity to achieve physical results. One would first have to perform the more realistic XMHD simulation to which the MHD simulation could be adjusted to fit the results. This reveals the advantage of XMHD over MHD since one can use the realistic Spitzer resistivity model without any artificial modifications, which allows the self-consistent and physical transition from high density to low density regions. Moreover, one should not conclude that including a vacuum resistivity into the MHD equations is sufficient to recover all of the effects of the Hall term. Suppression of low-density currents is only one effect of the Hall term. The Hall modification of the electric field cannot be modeled by a vacuum resistivity and can generate anode–cathode asymmetries [15], enhanced magnetic reconnection [4], and can lead to instabilities not present in MHD [24] or instabilities modified by the Hall term [20,21].

4.6.2. Magnetic reconnection

For magnetic reconnection to occur, a mechanism is required to break the flux-frozen-in condition, which could be resistivity, electron inertia, or anisotropic electron pressure [4]. In this section, we demonstrate the XMHD algorithm developed in this paper can solve the equations on the scale where electron inertia is important and yield results that are consistent with the full two-fluid model.

We initialize the problem using the GEM reconnection challenge initial conditions [4] modified appropriately for the XMHD model. The domain is $x \in (-12.8\lambda_i, 12.8\lambda_i)$, $y \in (-6.4\lambda_i, 6.4\lambda_i)$, speed of light is $c = 55v_A$, mass ratio is $m_i/m_e = 25$. The Harris sheet equilibrium is given by:

$$n(y) = \operatorname{sech}^2\left(\frac{y - L_y/4}{w_0}\right) + \operatorname{sech}^2\left(\frac{y + L_y/4}{w_0}\right) + 0.2$$

$$B_x(y) = \tanh\left(\frac{y + L_y/4}{w_0}\right) - \tanh\left(\frac{y - L_y/4}{w_0}\right) - 1.$$

We perturb the equilibrium as follows:

$$\delta B_x = -0.1 \frac{4\pi}{L_y} \cos\left(\frac{2\pi x}{L_x}\right) \sin\left(\frac{4\pi y}{L_y}\right)$$

$$\delta B_y = 0.1 \frac{2\pi}{L_x} \sin\left(\frac{2\pi x}{L_x}\right)\left[1 - \cos\left(\frac{4\pi y}{L_y}\right)\right]$$
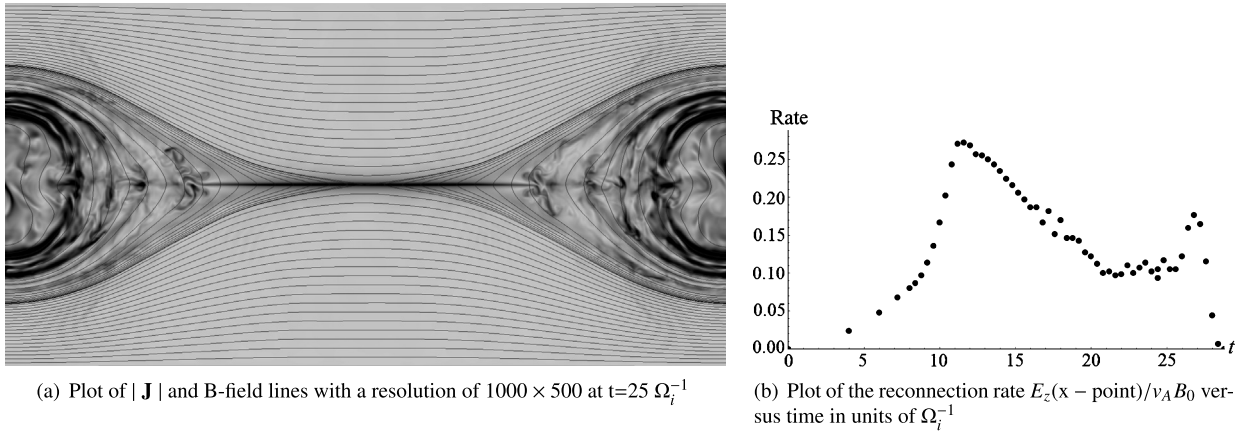
(a) Plot of $|\mathbf{J}|$ and B-field lines with a resolution of 1000×500 at t=25 Ω_i^{-1}

(b) Plot of the reconnection rate $E_z(\mathrm{x-point})/v_A B_0$ versus time in units of Ω_i^{-1}

Fig. 7. GEM challenge problem.

where $L_x = 25.6\lambda_i$, $L_y = 12.8\lambda_i$, and the initial current sheet thickness $w_0 = 0.5\lambda_i$. The simulation runs to $25\Omega_i^{-1}$ with a resolution of 800×400 cells. The legend values are based on the magnetospheric context for which we have chosen $B = 50$ nT, $n = 1 \times 10^6$ m^{-3}, $L_0 = 6 \times 10^5$ m, $v_A = 1.1 \times 10^6$ m s^{-1}. The time step and cell size are $\omega_{pe}\Delta t = 0.2$ and $\lambda_e/\Delta x = 6.1$.

The results with XMHD model is as shown in Fig. 7. In Fig. 7 we have added some numerical diffusion in the form of a slope limiter [18] to smooth the oscillations and limit the thinness of the current sheet. Although we are able to obtain stable results by doing this, the scheme with the slope limiter is no longer second order accurate. Even with slope limiting there is remarkable detail visible in the flows inside and the shocks outside the separatrix. This result compares very favorably with those of [16], who used a finite volume two-fluid code with a Riemann solver. The time history of the reconnection rate shown in Fig. 7(b) is consistent with [16] and with the results of [29] who used a particle-in-cell method.

We tested the global divergence of the magnetic field for this problem as computed from the second order finite difference of adjacent cell mean values normalized to the average magnitude of the magnetic field divided by the cell length. This measure of the global divergence is $\Gamma = \frac{1}{2}[B_{x0}(i+1,j) - B_{x0}(i-1,j) + B_{y0}(i,j+1) - B_{y0}(i,j-1)]/|B|$. We compared the results with the local structure preserving constraint applied to the same simulation without structure preserving. We find the range of values of Γ without structure preserving is $-0.033 < \Gamma < 0.033$ and with structure preserving is $-0.002 < \Gamma < 0.002$. Furthermore we observe that the run without structure preserving began to diverge significantly from the run with structure preserving around $t = 10\Omega_i^{-1}$ and was completely different at $t = 25\Omega_i^{-1}$ and therefore in complete disagreement with the results of [16] who used a divergence cleaning method to preserve div $B = 0$.

5. Concluding remarks

In this paper, we constructed a positivity-preserving DG scheme that solves an XMHD model. As constructed, the scheme is able to handle challenging problems having a large dynamic density range (from near-vacuum to solid density), which covers the entire density range of interest in HED plasma problems. Because the XMHD model is physically consistent from high densities to vacuum, it can properly treat the low-density regions, and eliminate the need for the non-physical vacuum resistivity required in MHD models.

The DG scheme has a number of distinct advantages for HED type problems: it is accurate for problems with δ-function discontinuities; step-type contact and shock discontinuities; and very importantly, boundary layers and small-scale structure variations due to non-MHD effects at the ion and electron inertial scales.

We have proven that the PP-limiter preserves the stability of a system governed by an XMHD model or an MHD model. This is essential, as the sharp transitions from a dense state of matter to near vacuum greatly stress any numerical method to keep the density, and in particular, the pressure positive. Also there is an advantage PP-limiter over TVD limiter, that is, it does not degrade the order of accuracy at smooth extrema.

We have shown that the XMHD equations can be solved by the DG method in the context of a relaxation system using an implicit–explicit scheme. This is a critical requirement since most HED problems evolve on time scales many orders of magnitude slower than the natural frequencies of the XMHD or two-fluid model. In order to solve HED problems using an XMHD model we must in practice step over the plasma frequency and electron cyclotron frequencies. We have demonstrated that the method presented in this paper succeeds well in this regard as we are able to accurately solve high-density problems with a time step that is many orders of magnitude larger than $1/\omega_{pe}$.

Acknowledgements

References

[1] D.S. Balsara, Second-order-accurate schemes for magnetohydrodynamics with divergence-free reconstruction, Astrophys. J. Suppl. Ser. 151 (1) (2004) 149.

[2] D.S. Balsara, Divergence-free reconstruction of magnetic fields and WENO schemes for magnetohydrodynamics, J. Comput. Phys. 228 (14) (2009) 5040–5056.

[3] D.S. Balsara, Self-adjusting, positivity preserving high order schemes for hydrodynamics and magnetohydrodynamics, J. Comput. Phys. 231 (22) (2012) 7504–7517.

[4] J. Birn, J.F. Drake, M.A. Shay, B.N. Rogers, R.E. Denton, M. Hesse, P.L. Pritchett, Geospace Environmental Modeling (GEM) magnetic reconnection challenge, J. Geophys. Res.: Space Phys. (1978–2012) 106 (A3) (2001) 3715–3719.

[5] M. Brio, C.C. Wu, An upwind differencing scheme for the equations of ideal magnetohydrodynamics, J. Comput. Phys. 75 (2) (1988) 400–422.

[6] L. Chacón, D.A. Knoll, A 2D high-β Hall MHD implicit nonlinear solver, J. Comput. Phys. 188 (2) (2003) 573–592.

[7] Y. Cheng, F. Li, J. Qiu, L. Xu, Positivity-preserving DG and central DG methods for ideal MHD equations, J. Comput. Phys. 238 (2013) 255–280.

[8] B. Cockburn, F. Li, C.W. Shu, Locally divergence-free discontinuous Galerkin methods for the Maxwell equations, J. Comput. Phys. 194 (2) (2004) 588–610.

[9] B. Cockburn, C.W. Shu, TVB Runge–Kutta local projection discontinuous Galerkin finite element method for conservation laws. II. General framework, Math. Comput. 52 (186) (1989) 411–435.

[10] B. Cockburn, S.Y. Lin, C.W. Shu, TVB Runge–Kutta local projection discontinuous Galerkin finite element method for conservation laws III: one-dimensional systems, J. Comput. Phys. 84 (1) (1989) 90–113.

[11] B. Cockburn, S. Hou, C.W. Shu, The Runge–Kutta local projection discontinuous Galerkin finite element method for conservation laws. IV. The multidimensional case, Math. Comput. 54 (190) (1990) 545–581.

[12] B. Cockburn, C.W. Shu, The Runge–Kutta discontinuous Galerkin method for conservation laws V: multidimensional systems, J. Comput. Phys. 141 (2) (1998) 199–224.

[13] S.A.E.G. Falle, S.S. Komissarov, P. Joarder, A multidimensional upwind scheme for magnetohydrodynamics, Mon. Not. R. Astron. Soc. 297 (1) (1998) 265–277.

[14] S.K. Godunov, A difference method for numerical calculation of discontinuous solutions of the equations of hydrodynamics, Mat. Sb. 89 (3) (1959) 271–306.

[15] P.A. Gourdain, C.E. Seyler, Impact of the Hall effect on high-energy-density plasma jets, Phys. Rev. Lett. 110 (1) (2013) 015002.

[16] A. Hakim, J. Loverich, U. Shumlak, A high resolution wave propagation scheme for ideal two-fluid plasma equations, J. Comput. Phys. 219 (1) (2006) 418–442.

[17] A.H. Hakim, Extended MHD modelling with the ten-moment equations, J. Fusion Energy 27 (1–2) (2008) 36–43.

[18] H. Hoteit, P. Ackerer, R. Mosé, J. Erhel, B. Philippe, New two-dimensional slope limiters for discontinuous Galerkin methods on arbitrary meshes, Int. J. Numer. Methods Eng. 61 (14) (2004) 2566–2593.

[19] J.D. Huba, Numerical methods: ideal and Hall MHD, in: Proceedings of ISSS, vol. 7, 2005 March, pp. 26–31.

[20] J.D. Huba, Hall dynamics of the Kelvin–Helmholtz instability, Phys. Rev. Lett. 72 (13) (1994) 2033.

[21] J.D. Huba, D. Winske, Rayleigh–Taylor instability: comparison of hybrid and nonideal magnetohydrodynamic simulations, Phys. Plasmas 5 (6) (1998) 2305–2316.

[22] R.J. LeVeque, Finite Volume Methods for Hyperbolic Problems, vol. 31, Cambridge University Press, 2002.

[23] F. Li, C.W. Shu, Locally divergence-free discontinuous Galerkin methods for MHD equations, J. Sci. Comput. 22 (1–3) (2005) 413–442.

[24] E. Liverts, M. Mond, The Hall instability in accelerated plasma channels, Phys. Plasmas 11 (1) (2004) 55–61.

[25] J. Loverich, U. Shumlak, A discontinuous Galerkin method for the full two-fluid plasma model, Comput. Phys. Commun. 169 (1) (2005) 251–255.

[26] M. Martin, Generalized Ohm's law at the plasma–vacuum interface, Doctoral dissertation, Cornell University, 2010.

[27] D.D. Schnack, Lectures in Magnetohydrodynamics: With an Appendix on Extended MHD, vol. 780, Springer, 2009.

[28] C.E. Seyler, M.R. Martin, Relaxation model for extended magnetohydrodynamics: comparison to magnetohydrodynamics for dense Z-pinches, Phys. Plasmas 18 (2011) 012703.

[29] M.A. Shay, J.F. Drake, M. Swisdak, Two-scale structure of the electron dissipation region during collisionless magnetic reconnection, Phys. Rev. Lett. 99 (15) (2007) 155002.

[30] C.R. Sovinec, D.D. Schnack, A.Y. Pankin, D.P. Brennan, H. Tian, D.C. Barnes, S.C. Jardin, Nonlinear extended magnetohydrodynamics simulation using high-order finite elements, J. Phys. Conf. Ser. 16 (1) (2005 January) 25.

[31] B. Srinivasan, A comparison between the discontinuous Galerkin method and the high resolution wave propagation algorithm for the full two-fluid plasma model, Doctoral dissertation, University of Washington, 2006.

[32] B. Srinivasan, A. Hakim, U. Shumlak, Numerical methods for two-fluid dispersive fast MHD phenomena, Commun. Comput. Phys. 10 (1) (2011) 183.

[33] C.W. Shu, S. Osher, Efficient implementation of essentially non-oscillatory shock-capturing schemes, J. Comput. Phys. 77 (2) (1988) 439–471.

[34] U. Shumlak, J. Loverich, Approximate Riemann solver for the two-fluid plasma model, J. Comput. Phys. 187 (2) (2003) 620–638.

[35] H. Trac, U.L. Pen, A primer on Eulerian computational fluid dynamics for astrophysics, Publ. Astron. Soc. Pac. 115 (805) (2003) 303–321.

[36] B. Van Leer, Towards the ultimate conservative difference scheme. V. A second-order sequel to Godunov's method, J. Comput. Phys. 32 (1) (1979) 101–136.

[37] Y. Yang, I. Roy, C.-W. Shu, L.-Z. Fang, The angular distribution of Lyα resonant photons emerging from an optically thick medium, Astrophys. J. 772 (1) (2013) 3.

[38] Y. Yang, C.W. Shu, Discontinuous Galerkin method for hyperbolic equations involving delta-singularities: negative-order norm error estimates and applications, Numer. Math. (2013) 1–29.

[39] Y. Yang, D.M. Wei, C.W. Shu, Discontinuous Galerkin method for Krause's consensus models and pressureless Euler equations, J. Comput. Phys. 252 (2013) 109–127.

[40] S. Zahedi, A.K. Tornberg, Delta function approximations in level set methods by distance function extension, J. Comput. Phys. 229 (6) (2010) 2199–2219.

[41] X. Zhang, C.W. Shu, A genuinely high order total variation diminishing scheme for one-dimensional scalar conservation laws, SIAM J. Numer. Anal. 48 (2) (2010) 772–795.

[42] X. Zhang, C.W. Shu, On positivity-preserving high order discontinuous Galerkin schemes for compressible Euler equations on rectangular meshes, J. Comput. Phys. 229 (23) (2010) 8918–8934.